Drug Delivery

http://informahealthcare.com/drd
ISSN: 1071-7544 (print), 1521-0464 (electronic)

Drug Deliv, 2017; 24(1): 660–669
 DOI: 10.1080/10717544.2017.1303854

Taylor & Francis
Taylor & Francis Group

RESEARCH ARTICLE

Honokiol-loaded polymeric nanoparticles: an active targeting drug delivery system for the treatment of nasopharyngeal carcinoma

Bo Yang[1], XiaoLing Ni[1], LongXia Chen[1], Heng Zhang[1], PeiRong Ren[1], Yue Feng[2], Yue Chen[2], ShaoZhi Fu[1], and JingBo Wu[1]

[1]*Department of Oncology, the Affiliated Hospital of Southwest Medical University, Luzhou, China and* [2]*Department of Nuclear Medicine, the Affiliated Hospital of Southwest Medical University, Luzhou, China*

Abstract

The purpose of this study was to develop a novel drug delivery system for a sustained and targeted delivery of honokiol (HK) to the nasopharyngeal carcinoma (NPC) HNE-1 cell lines, since the folate receptor (FR) is over-expressed on their surface. Emulsion solvent evaporation was used to develop the active targeting nanoparticles-loaded HK (ATNH) using copolymerpoly (ε-caprolactone)-poly (ethyleneglycol)-poly (ε-caprolactone) (PCEC), which was modified with folate (FA) by introducing Polythylenimine (PEI). ATNH characterization, including particle size distribution, morphology, drug loading, encapsulation efficiency and drug release, was performed. Transmission electron microscopy (TEM) and Fourier transform infrared spectroscopy (FTIR) were employed to evaluate the shape and construction, respectively. MTT assay, cell uptake study and apoptosis test were assayed to detect the antitumor properties and targeting uptake by HNE-1 cells *in vitro*. Cell-cycle redistribution, ^{18}F-FDG PET/CT and immunohistochemistry were performed *in vivo*. The ATNH we developed were successfully synthesized and showed a suitable size distribution, high encapsulation efficiency, gradual release, and targeting uptake by the cells *in vitro*. Moreover, ATNH significantly inhibited tumor growth, metabolism, proliferation, micro-vessel generation, and caused cell-cycle arrest at G_1 phase. Thus, these nanoparticles we developed might represent a novel formulation for HK delivery and a promising potential therapy in the treatment of cancer.

Keywords

Honokiol, active targeting, nanoparticles, folate, NPC

History

Received 24 October 2016
Revised 17 January 2017
Accepted 22 January 2017

Introduction

Over the past decades, considerable attention has been focused on the development of nanosized drug delivery systems for Chinese herbal medicines (Shi et al., 2013a). Honokiol (HK) is one of the major phenolic constituents isolated from the root and stem bark of *Magnolia officinalis* (Li et al., 2008). It has several pharmacological effects and has been used for centuries as folk medicine by the Chinese traditional medicine to treat many diseases such as thrombotic stroke, gastrointestinal complaints, anxiety, and nervous disturbance (Deng et al., 2008; Li et al., 2008; Fried & Arbiser, 2009). Recently, HK has been reported to induce apoptosis in several cancer cell lines (Wang et al., 2004; Liu et al., 2008; Jeong et al., 2012; Zhang et al., 2015a). Moreover, HK has a remarkable *in vivo* antitumor activity against oral squamous tumors and human head and neck squamous cell carcinoma by targeting epidermal growth factor receptor (Cho et al., 2015; Singh et al., 2015). However, its use is limited mostly because of its poor water solubility (Zheng et al., 2010).

''Nanomedicine'' has recently received extensive attentions for the application of nanotechnology in diagnosis, monitoring, disease therapy, and control of biological systems (Gou et al., 2008). After the drug is loaded into nanoparticles, it can be released from the nanoparticles in a controlled and sustained manner. Moreover, nanoparticles can passively enter into solid tumors due to their enhanced permeability and retention (EPR) effect, which results in higher drug concentration in tumor that make anti-cancer drug more efficient (Gou et al., 2009). Therefore, HK encapsulation into nanopolymers to obtain well-dispersed drug slurry was performed to overcome the water solubility problem of the hydrophobic drug HK. Due to its biodegradability, good biocompatibility, low toxicity, amphiphilic property, and ease to produce, PCEC is a novel candidate for injectable drug delivery system (Gou et al., 2009). Hence, we developed the ATNH using PCEC by emulsion solvent evaporation method.

Address for correspondence: ShaoZhi Fu and JingBo Wu, Department of Oncology, the Affiliated Hospital of Southwest Medical University, Luzhou 646000, China. Tel: +86 830 3165690. Fax: +86 830 3165690. Email: shaozhifu513@163.com(S. F.); wjb6147@163.com (J. W.)

FR is a glycosyl phosphatidylinositol-anchored membrane protein, which is over-expressed in more than 90% of ovarian carcinomas and in other epithelial cancers to varying degrees. The distinct expression pattern of FR between normal and malignant tissues makes it an ideal target for drug delivery (Huang et al., 2014). A recent study showed that FR is over-expressed in the HNE-1 cell lines (Xie et al., 2013). According to the International Agency for Research on Cancer, NPC accounts for 86 700 new cases and 50 800 deaths in 2012(Torre et al., 2015). At present, radiotherapy is the primary treatment modality for non-disseminated nasopharyngeal carcinoma due to its anatomical location and radio-sensitivity (Chen et al., 2012). Thus, ATNH could represent a potential valid treatment alternative.

A recent study showed the successful use of MPEG-PCL-g-PEI micelles for co-delivering a functional gene and chemotherapeutic agent (Shi et al., 2014). For this reason, we introduced PEI into the PCL core of the PCEC to conjugate the folate to perform a preliminary study which developing a carry system to targeting delivery the functional gene and chemotherapeutic at the same time. Hence, the purpose of this study was to develop an active targeting delivery system which could simultaneously increase the therapeutic effect.

Materials and methods

Materials, cell lines, and animals

HK (≥99%) was purchased from MeiLun Co. Ltd (Dalian, China). Dicyclohexylcarbodiimide (DCC), polythylenimine (PEI), *N*-hydroxysuccinimide (NHS), fluorescein isothiocyanate (FITC), and 3-(4,5-dimethylthiazol-2-yl)-2,5-diphenyltetrazolium bromide (MTT) were purchased form Sigma-Aldrich (St. Louis, MO). Tetrahydrofuran (THF) was purchased from Bioway (New York, NY). Dimethyl sulfoxide (DMSO) and acetonitrile (HPLC grade) were purchased from Kelong Co. Ltd. (Chengdu, China).

Human nasopharynx carcinoma cells (HNE-1) were provided by the Shanghai LeiDi biotechnology Co. Ltd. (Shanghai, China). HNE-1 cells were grown in RPMI medium (1640, Gibco, Waltham, MA) supplemented with 10% fetal bovine serum (FBS, Gibco, Waltham, MA) at 37 °C in a humidified incubator containing 5% CO_2.

BALB/c mice (female, nu/nu, 4 weeks old) were provided by Chongqing TengXin biotechnology Co. Ltd. (Chongqing, China), fed with standard laboratory chow and tap water *ad libitum* and housed at a controlled temperature of 20–22 °C, with a relative humidity of 50–60% and 12 h light-dark cycles. All animals' procedures were performed following the protocol approved by the Institutional Animal Care and Treatment Committee of Southwest Medical University (Luzhou, China). All mice were treated humanely throughout the experimental period.

Synthesis and characterization of FA-conjugated PCEC

PCEC ($M_w = 3700$) copolymers used in this study were synthesized by ring-opening polymerization of ε-CL on PEG (2000) using Sn $(Oct)_2$ as a catalyst, as a previously report (Gou et al., 2010). Next, PCEC-FA copolymer synthesis was carried out using a two-step reaction. First, activated PCEC was obtained by mixing 1.2 mM DCC and 1.2 mM NHS with 0.37 mM PCEC in 30 mL THF under magnetic stirring at 3000 rpm for 4 h at room temperature. Then, the activated PCEC was mixed with 4.0 mM PEI solution under magnetic stirring for 1 h at the same temperature. The precipitate was discarded by filtration using 0.45 μm Teflon filter paper. The polymer product was precipitated in 120 mL petroleum ether under vigorous stirring and was dissolved in 100 mL methanol, then dialyzed against deionized water at 4 °C for 72 h, freeze-dried, and stored at −60 °C. Second, similarly, 0.3 mM FA was activated using 1.2 mM NHS and 1.2 mM DCC and reacted with 0.3 mM PCEC-PEI to obtain PCEC-PEI-FA copolymer at the similarly condition.

Preparation of ATNH

ATNH was prepared by emulsion solvent evaporation method (Gou et al., 2008). HK (4 mg) and PCEC-PEI-FA copolymer (46 mg) were dissolved in 4 mL of methanol to form the organic phase. Then the organic phase was dropped into water under moderate mechanical stirring. After stirring in magnetic apparatus for 6 min, the oil in water (O/W) emulsion was obtained. Subsequently, the methanol and water were evaporated using a rotator evaporator. At the end of the formulation, 20 mL ultrapure water was used to dissolve and washed the nanoparticles at 45 °C and then the ATNH were obtained. The blank vehicle nanoparticles (BVN) and the non-active targeting nanoparticles-loaded HK (NATNH) which did not modified with FA were developed with the similarly method.

Characterization of ATNH

ATNH size was determined by dynamic light scattering (DLS, NanoBrook90 plus Zeta, Brookhaven, Cambridge, MA) at 25 °C by dissolving in ultrapure water. Three separated tests were performed. ATNH morphology was investigated using transmission electron microscope (TEM, Tecnai G2 F 20, Hillsboro, OR).

Fourier transform infrared (FTIR) spectroscopy

FTIR (KBr) spectroscopy was performed at room temperature to detect FA in the synthesized copolymer, using a NICOLET 200SXV Infrared Spectrophotometer (Rhinelander, WI). The characteristic absorption bands of the drug and polymer were detected in samples including BVN, FA, and ATNH.

Determination of drug loading (DL) and encapsulation efficiency (EE)

To determine ATNH DL and EE, the amount of HK in the ATNH was measured using high-performance liquid chromatography (HPLC, Agilent, Richardson, TX) instrument, with a reverse phase C18 column (4.6 × 150 mm, 3.5 μm particle size) through the method reported (Zheng et al., 2010). The ATNH were dissolved in the mobile phase, which contained acetonitrile/water (60/40, v/v), which disrupted the nanoparticles and enabled free HK to be determined. The HPLC was

performed with a flow rate of 1.0 mL/min, a column temperature of 28 °C and a detection wavelength of 254 nm. EE and DL were calculated according to the following equations:

$$EE = \frac{\text{Experimental drug loading}}{\text{Theoretical drug loading}} \times 100\% \quad (1)$$

$$DL = \frac{\text{Drug}}{\text{Polymer + Drug}} \times 100\% \quad (2)$$

HK *in vitro* release

HK *in vitro* release from ATNH was evaluated using a modified dialysis method (Gou et al., 2009). One mL ATNH solution was placed in a dialysis bag (MWCO: 3.5 kDa), and 1 mL HK solution in absolute ethyl alcohol (0.5 mg/mL) was used as control. The dialysis membrane was immersed in 40 mL PBS (0.01 M, pH 7.4) at 37 °C ± 0.5 containing Tween80 (0.5%, wt%) under constant and gentle stirring. Periodically, 2 mL aliquots of the dialysis medium were removed and replaced with the same volume of fresh medium. All samples were analyzed using HPLC. Each experiment was carried out in triplicate.

NPs cellular uptake

FITC-labeled PCEC-PEI, PCEC-PEI-FA, and PCEC-PEI-FA nanoparticles were prepared by dropping FITC ethanol solution into 1.0 mg/mL of PCEC-PEI-FA nanoparticles solution (Zhou et al., 2010). PCEC-PEI-FA nanoparticles to FITC molar ratio was maintained at 1:4. The solution was stirred for 24 h at 400 rpm at room temperature in lucifuge environment. The reaction product was dialyzed against ultrapure water for 24 h using a dialysis membrane (MWCO: 3.5 kDa, Spectrum Laboratories, Richardson, TX) to remove the un-reacted FITC.

HNE-1 cells were seeded at 10^5 mL^{-1} cells/well in a 24-well plate and incubated for 24 h. Fifty μL medium containing 10 μg/m FITC-PPF nanoparticles or FITC-PPF were added and the cells were incubated for 2 h. For comparison, free FA dissolved in DMSO was added into the fresh medium containing FITC-PPF nanoparticles at the concentration 10 μg/mL. After washing with PBS (0.01 M, pH 7.4) three times, the cells were observed by fluorescence microscopy (Olympus, Tokyo, Japan).

Cytotoxicity assay

Cytotoxicity assay was performed as previously described (Wang et al., 2004). HNE-1 cells were seeded in 96-well plate and incubated for 24 h at 37 °C, then exposed to free HK, BVN, NATNH, and ATNH at different concentrations (ranging from 0 to 40 μg/mL) for 24 h. Cell viability was evaluated by MTT and analyzed and recorded at 490 nm using a microplate reader (iMark, Bowie, MD).

Cell apoptosis analysis

HNE-1 cells in 1 mL were seeded in six-well plates at a density of 50 000 cells per well. At 60% confluence, the culture medium was replaced by fresh culture medium containing 40 μM HK, BVN, NATNH, and ATNH. Drug-treated cells were incubated for 24 h. Floating and adherent cells were collected and centrifuged at 2000 rpm for 5 min to discard the supernatant. Cells were washed three times with normal saline (NS) and NS to reach a density of 10^5 cells per mL. Sample were dyed with propidium iodide (PI) and Annexin V-FITC and apoptosis was evaluated by flow cytometry instrument (BD FACSVerse, Piscatway, NJ) (Zhang et al., 2015b).

Nude mouse xenograft

Mouse HNE-1 xenograft model was obtained by subcutaneous injection of HNE-1 cells (10^6 cells in 100 μL PBS/animal) into the right dorsal aspect of the right foot of athymic nude mice (18 g ± 2). When the tumors had reached an average volume of 100–200 mm^3, animals were randomly assigned to the following five groups ($n = 12$): control (saline), BVN, free HK, NATNH, and ATNH. Subsequently, each mouse of honokiol-treated group received 3 mg/kg every 3 d of HK suspended in PEG 1500/glucose (1:1 by volume) by intravenous injection. The NATNH and the ATNH group received NATNH and ATNH obtained equal HK suspended in saline. The BVN group received equal blank vehicle nanoparticles. After four times treatment, 50% of the animals in each group were randomly euthanized for cell-cycle analysis and immunochemistry studies. The remaining mice were under observation for tumor growth and survival time. The tumors were measured along the two diameter axes using the calipers and the volume was estimated by the following equation: $V = D \times d^2/2$, where D and d were the larger and smaller diameters, respectively. Tumor growth curve (TGC) was calculated with (Ti_{10}–T_{10}) as the time taken for the treated tumors (Ti_{10}) and the control tumors (T_{10}) to multiply their initial tumor volume 10-fold. At the end of the experiment, tumors were removed for flow cytometry and immunohistochemical analysis.

FDG PET/CT imaging and quantitative imaging analysis

^{18}F-FDG PET/CT is an accurate technique for cancer detection, staging, and monitoring of therapy in patients with various malignant cancer (Younes-Mhenni et al., 2004; Cho et al., 2015). Micro animal ^{18}F-FDG PET/CT imaging was performed to evaluate the early response of tumor tissue in mice to free HK, NATNH, and ATNH, using anInveon micro PET/CT (Siemens, Münch, Germany) animal scanner. At the third day after the last (fourth) treatment with HK, NATNH, and ATNH, mice were put underwent fasting conditions 6 h and anesthetized with 1% (5 mL/Kg) pentobarbital. Animal-PET/CT scans and image analyses were performed 1 h after injection of radio-labeled tracer (intraperitoneal injection of 200–300 μCi ^{18}F-PDG). Animals were maintained under 2% isoflurane anesthesia during the scanning period. The parameters used were as follows: 80 kV, 500 μA, slice thickness 1.5 mm, and 10 min per bed position.

The animal-PET and animal-CT images were generated separately and then merged. The irregular region of interest

(ROI) was manually drawn covering the whole tumor on the merged images plane with the largest tumor appearance. In addition, ROIs were drawn on the opposite paraspinal muscles. The uptake value of the tracer in the tumor and muscle tissue was recorded in the attenuation-corrected transaxial tomographic slices, by calculating the standard uptake value (SUV) in a given ROI. In order to calculate the tumor/muscle (*T*/*M*) ratio, the maximal SUVs for ^{18}F-FDG were obtained from the selected ROI and compared with the SUVs of the opposite paraspinal muscles.

Cell-cycle analysis

Soya bean size tumor tissues specimens harvested from nude mice were cut into pieces and then immediately mixed with 200 µL of 0.25% trypsin/EDTA (1:1, v/v), stirred for 1 min at room temperature and then filtered using a 70-µm nylon net. Tumor cells were collected including those floating in the medium. Cell suspensions were centrifuged for 3 min at 1500 rpm at room temperature, then washed three times with saline and fixed with 70% ethanol at 4 °C overnight. All samples were washed three times with PBS (0.01 M, pH 7.4) and resuspended in propidium iodide (PI) (50 µg/mL) (Keygen, Nanjing, China) and RNaseA (20 µg/mL) in PBS for 30 min at room temperature. Stained cells were analyzed by flow cytometry (BD FACSVerse, Piscatway, NJ).

Immunohistochemistry (IHC)

Tumor tissues were fixed in 10% neutral buffered formalin solution, embedded in paraffin, and cut into 4 µm thick sections for IHC. Routine hematoxylin and eosin (HE) staining was performed to facilitate histological evaluation. Ki-67 and CD31 expressions were evaluated according to the manufacturer's instructions (Bioworld Technology, Nanjing, China) and the photos were taken using an optical microscope (Olympus, Tokyo, Japan). The Ki-67 was calculated in five randomly selected areas (at ×200 magnification) in each tumor sample as the number of positive cells/total counted. Tumor tissue micro-vessel density (MVD) was calculated as the mean value of the CD-31-positive micro-vessels using the same calculation explained above.

Statistical analysis

Statistical analysis was carried out using SPSS 17.0 software (SPSS Inc., Chicago, IL). All the data were expressed as the mean ± standard deviation (SD). Data were analyzed using a one-way analysis of variance (ANOVA) when more than two groups were compared. Survival curves were generated according to the Kaplan–Meier method. Means were considered different at $p < 0.05$ and statistically significantly $p < 0.01$.

Results

ATNH preparation and characterization

ATNH morphology and size were evaluated by DLS and TEM. Figure 1(A) shows a typical DLS image of ATNH, which indicated that the prepared nanoparticles were spherical, with a mean diameter of 188.34 nm ± 0.54 (polydispersity index (PDI) = 0.21). The obtained ATNH were mono-dispersed and stable in water solution. Further measurement of particle size was evaluated by TEM. Figure 1(B) reveals an average hydrodynamic diameter of 20.77 nm ± 7.56.

The molecular structures of PCEC and FA copolymers were confirmed by FTIR spectroscopy (Figure 1C). In the spectrum of PCEC-PEI-FA copolymer, the absorption band

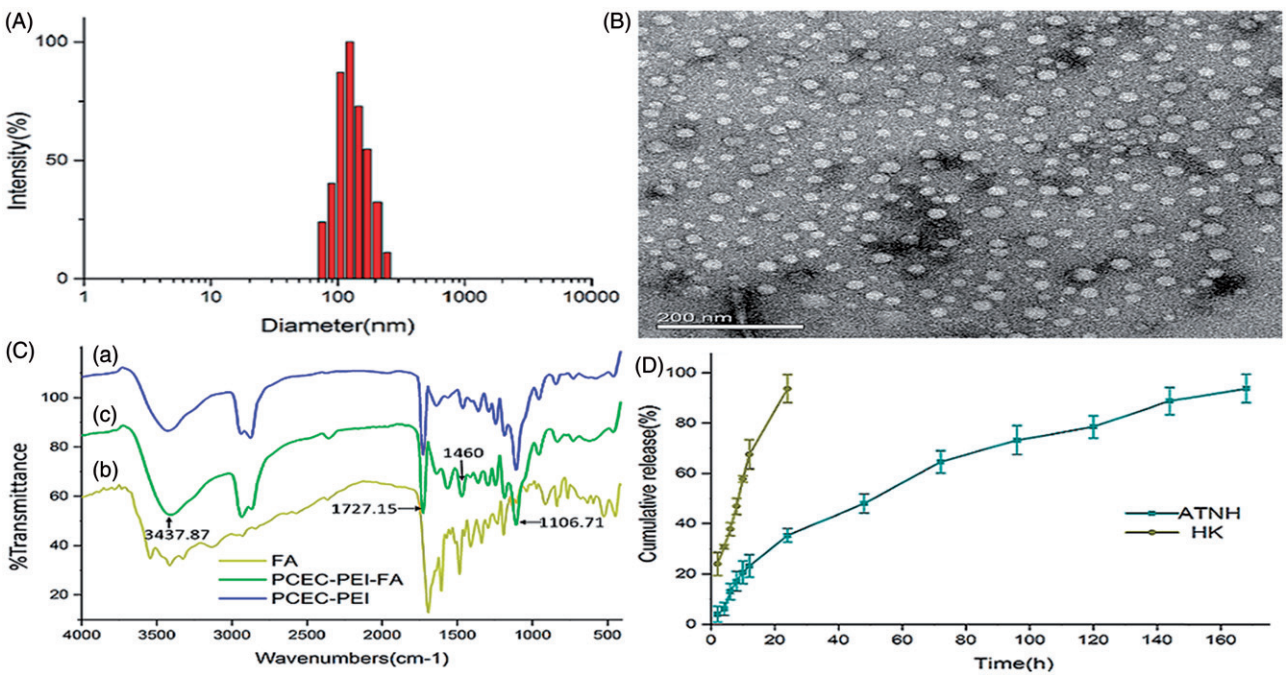

Figure 1. The characterization of ATNH. (A) The particles size distribution of ATNH. (B) The TEM image of ATNH. (C) The Fourier transform infrared (FTIR) spectrum of (a) PCEC-PEI, (b) FA, and (c) PCEC-PEI-FA. (D) *In vitro* release profile of HK from ATNH in PBS (PH = 7.4) at 37 °C.

at 3437.87 cm^{-1} was due to terminal hydroxyl groups (−OH) of the PCEC chains. The absorption bands at 1106.71 cm^{-1} belonged to the characteristic C–O–C stretching vibrations of repeated $–OCH_2CH_2$ units of PEG block. The characteristic band at 1727.15 cm^{-1} was attributed to C = O stretching vibrations of the ester carbonyl (Fu et al., 2011). PCEC-PEI-FA displayed an absorbance peak at 1460 cm^{-1} corresponding ρ-amino benzoic acid of FA (Shi et al., 2013b).

DL, EE, and *in vitro* release

In this study, the theoretical DL in the copolymers was set as 8%. However, according to the HPLC results, ATNH showed a DL of 6.26% ± 0.04, while EE was 78.25% ± 0.41 for HK. *In vitro* release study showed that free HK exhibited a rapid release and almost complete within 24 h (Figure 1(D)). In contrast, ATNH showed a much slower cumulative release rate, and no burst HK release from ATNH was observed. Indeed, approximately 150 h were required to release 90% of HK in the medium from the ATNH group.

Cytotoxicity assay and cell uptake

Figure 2(A(a)) illustrates the dose-dependent inhibitory effect of free HK, NATNH, and ATNH on HNE-1 cells. ATNH exerted the strongest inhibitory effect compared with free HK and NATNH ($p < 0.01$). In addition, ATNH and NATNH cytotoxicity was higher than free HK independently of whether it was conjugated to FA or not. This result implied that HK therapeutic effect was significantly improved when encapsulated into NPs. HK IC50 was 38.59 μg/mL after 24 h incubation, while ATNH IC50 was 18.41 μg/mL, indicating that the therapeutic effect of HK was enhanced when HK was incorporated into ATNH. The cytotoxicity of BVN without HK was also evaluated. Figure 2(A(b)) shows showed a negligible cytotoxic effect at all the tested concentrations, indicating that the anti-tumor activity of ATNH can be attributed to HK released from the nanoparticles. Thus, BVN could be used as a safe drug delivery carrier.

HNE-1 fluorescence images after incubation with either FITC-labeled PCEC-PEI or PCEC-PEI-FA nanoparticles are shown in Figure 2(B). In the control group, no fluorescence spot was observed (Figure 2B(a)). The fluorescence intensity of FITC-labeled PCEC-PEI-FA was more remarkable than that of FITC-labeled PCEC-PEI, suggesting that FA-conjugated agent display a better rate of cellular uptake than the unconjugated (Figure 2B(b and c)). The fluorescence intensity of FITC-labeled PPF NPs was actually the most remarkable, compared with other agents, suggesting that FA-conjugated nanoparticles displayed the best rate of cellular uptake (Figure 2B(b–d)). However, lower fluorescence intensity was observed following the addition of free FA into the medium containing FITC-labeled PCEC-PEI-FA nanoparticles (Figure 2B(e)), suggesting that free FA prevented PCEC-PEI-FA nanoparticles entrance into HNE-1 cells due to competitive binding to FR on the cell surface. These results indicated that FA-conjugated nanoparticles might be a potential drug carrier targeting tumor cells through FR-mediated endocytosis.

ATNH *in vivo* antitumor efficacy

Tumor volume in mice after different treatments was measured and plotted as shown in Figure 3(A). The tumor growth delay was 8 d ($p < 0.05$) in the mice treated with HK. NATNH was more effective than HK, with a tumor delay of

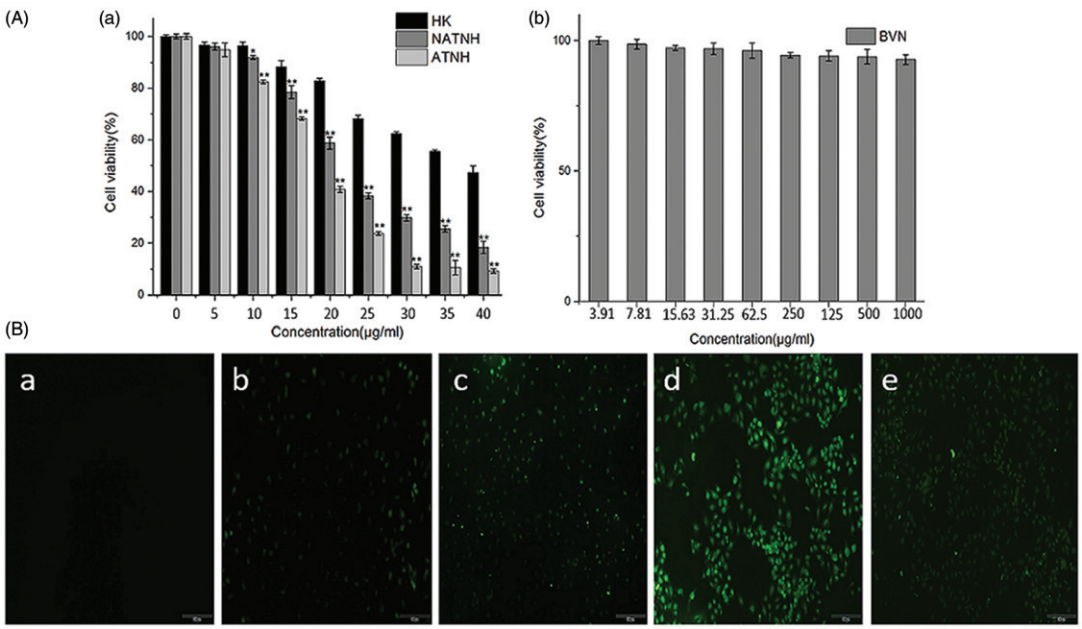

Figure 2. Cytotoxicity studies on HNE-1cells after different treatment. (A) (a) *In vitro* cell viability of free HK, NATNH and ATNH on HNE-1 cell after 24 h incubation; (A) (b) *in vitro* cell viability of BVN. *$p < 0.05$ and **$p < 0.01$, ATNH and NATNH relative to free HK. Fluorescent images of HNE-1 cells treated with medium B(a), FITC-labeled PCEC-PEI B(b), FITC-labeled PCEC-PEI-FA B(c), FITC-labeled PCEC-PEI-FA nanoparticles B(d), and FITC-labeled PCEC-PEI-FA nanoparticles + FA B(e) for 2 h.

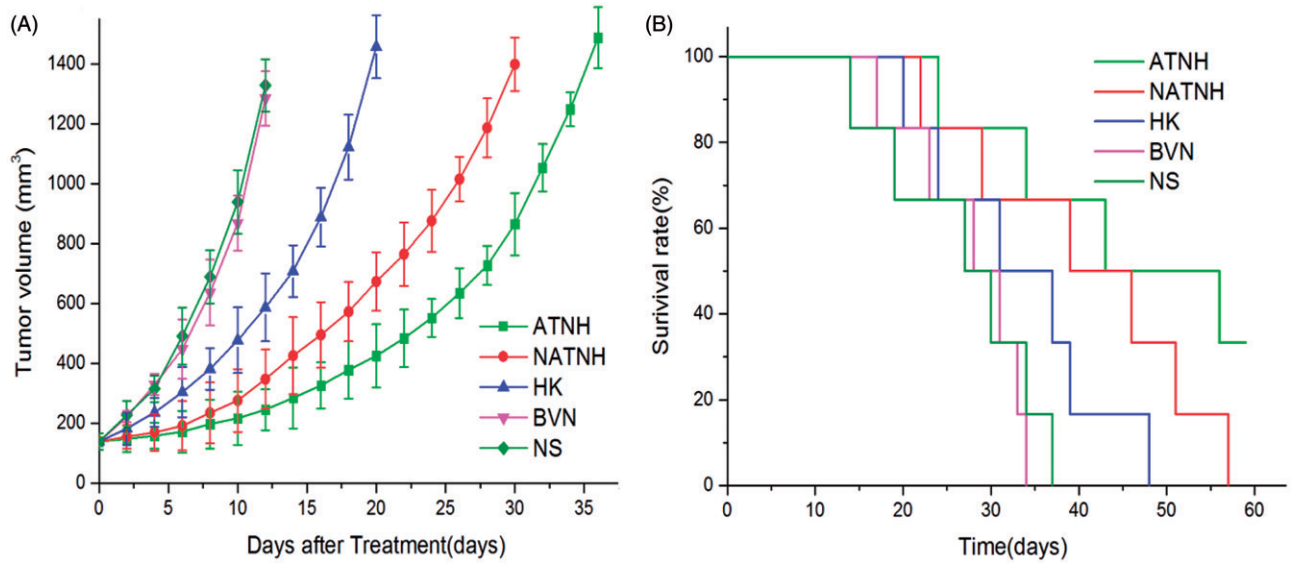

Figure 3. ATNH inhibited tumor growth in subcutaneous HNE-1 model. (A) Suppression of subcutaneous tumor growth by ATNH in mice. (B) Survival curve of mice in each group.

Figure 4. The representative ^{18}F-FDG PET/CT images of the mice at the third day after the last (fourth) treatment.

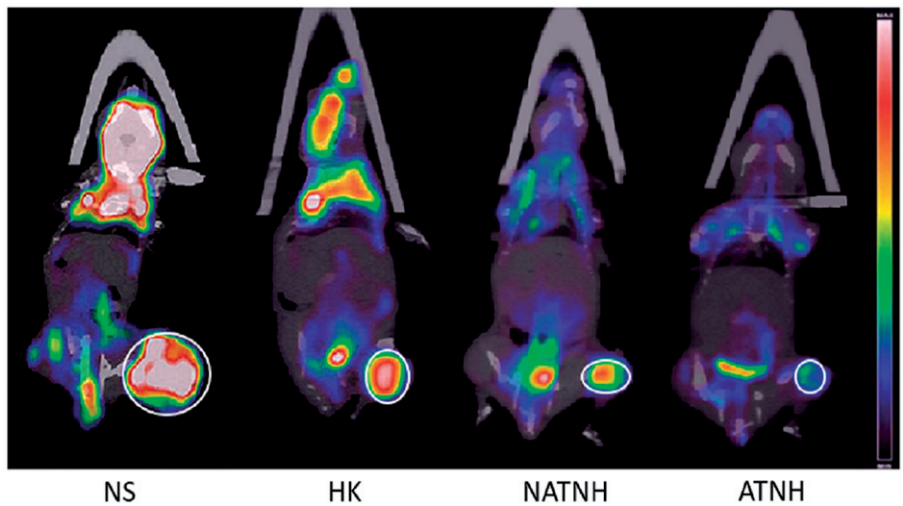

18 d ($p < 0.01$), while ATNH showed the longest tumor delay of 24 ds ($p < 0.01$).

To determine ATNH therapeutic effect, the median survival time was compared among the different treatments (Figure 3(B)). In the saline control group, the median survival time was 28.5 d, while it was 29.5 d in the BVN group ($p > 0.05$). A slight increase of 34 d in mice median survival time was observed when treated with HK. The median survival time of the NATNH group was 42.5 d. The ATNH group showed a median survival time of 57.5 d.

Micro ^{18}F-FDG PET/CT imaging

A remarkable difference in T/M values among the four groups ($p < 0.01$) was observed (Figure 4): NS group 5.24 ± 1.86, HK group 3.32 ± 1.54, NATNH group 2.18 ± 0.91, and ATNH group 1.03 ± 0.42. Indeed, all the treatment groups showed a remarkable decrease in T/M value compared with the control group (NS). The T/M value in ATNH group was the lowest, suggesting the best tumor response compared with HK and HPP nanoparticles.

Cell-cycle and cell apoptosis studies

Figure 5(A) shows the cells amount at different phases of the cell cycle (G_1 phase, S phase, and G_2/M phase). A remarkable increase of cells in the G_1 phase in the ATNH group ($51.24\% \pm 3.95$) was observed compared with the NATNH group ($45.92\% \pm 2.75$, $p < 0.01$) and the HK group ($37.43\% \pm 4.26$, $p < 0.05$). Figure 5(C(a)) shows quantitative analysis of the cell-cycle phase percentage.

In Figure 5(B), UR, LL, and LR represent late apoptotic and dead cells, live cells, and early apoptotic cells, respectively. Quantitative analysis showed that the percentage of apoptotic cells were as follows (Figure 5C(b)): NS group $7.60\% \pm 1.01$, BVN group $13.65\% \pm 2.08$, HK group $55.75\% \pm 1.02$, NATNH group $70.89\% \pm 3.76$, and ATNH group $86.07\% \pm 4.95$. BVN showed a mild effect on HNE-1

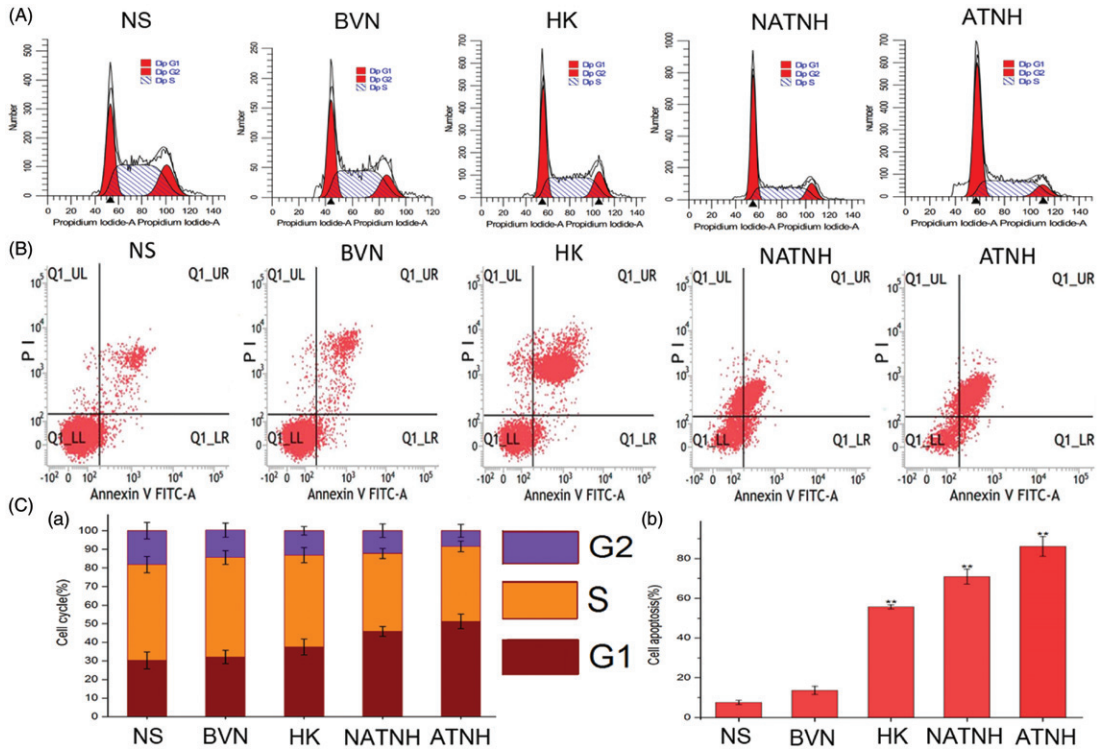

Figure 5. Cell apoptosis (A), cell-cycle phase analyze (B). Quantitative analysis of the percentage of cells in G_1, S, and G_2/M phase (C (a)) and the percentage of apoptosis cells (C (b)) in various groups. *$p < 0.05$ and **$p < 0.01$, ATNH, NATNH, and free HK relative to NS.

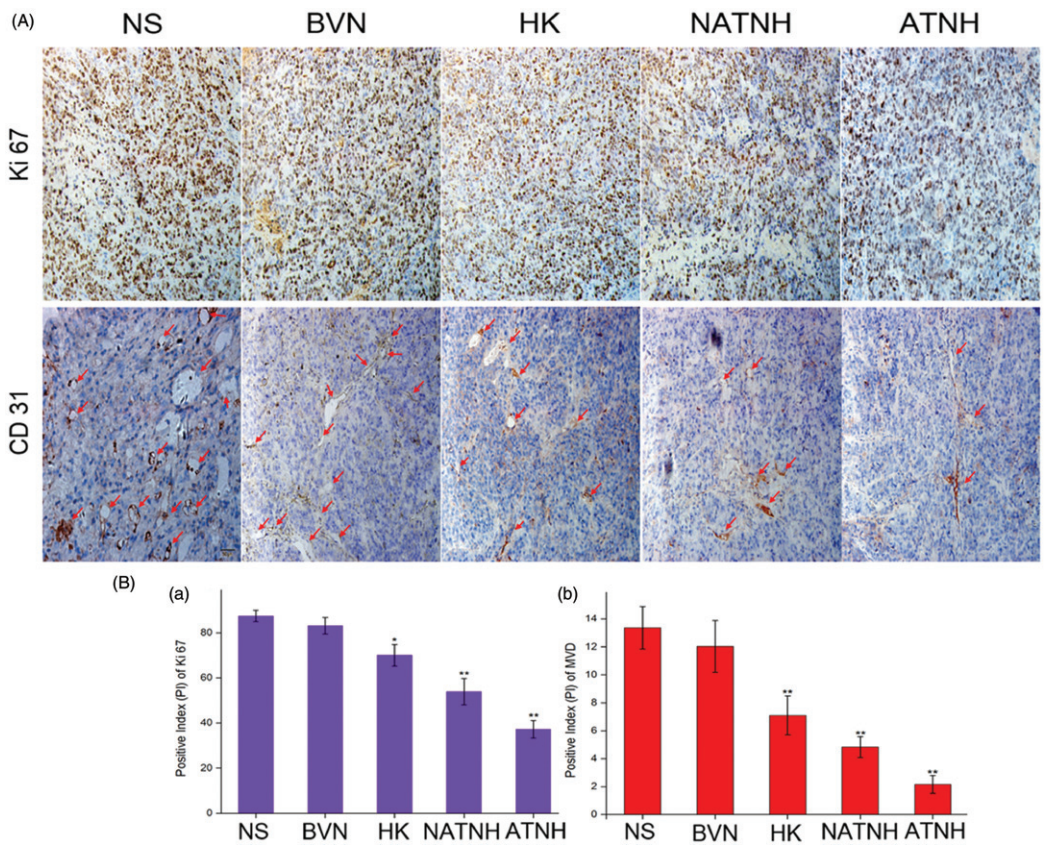

Figure 6. Immunohistochemical analysis of tumor tissue from mice that received different treatment. (A) Representative immunohistochemical images of tumor tissue from mice in various group. (B (a)) and (B (b)) represent the quantitative analysis of Ki 67 and CD 31 expression in xenografts from mice in various group, respectively. The red arrows indicate the positive expression of CD 31. *$p < 0.05$ and **$p < 0.01$, ATNH, NATNH, HK and BVN relative to NS group. Original magnification, ×200.The quantitative analysis was performed with IPP. (See color figure in the online version.)

apoptosis ($p > 0.05$), indicating a good biocompatibility of the carrier. HNE-1 total cell death rate (UR + LR) due to ATNH was higher than that of HK and NATNH (Figure 5B) ($p < 0.01$). These results were consistent with our *in vitro* cytotoxicity results.

Immunohistochemistry (IHC)

ATNH significantly reduced Ki 67 and CD31 expression (Figure 6A). Figure 6(B(a)) shows the percentage of Ki 67 positive cells in the ATNH group ($37.24\% \pm 3.89$, $p < 0.01$), NATNH group ($53.89\% \pm 5.84$, $p < 0.01$), HK group ($70.04\% \pm 4.76$, $p < 0.05$), BVN group ($83.12\% \pm 3.63$, $p > 0.05$), and NS group ($87.42\% \pm 2.53$). Figure 6(B(b)) shows that the CD31 expression level in the ATNH group was 2.16 ± 0.76 ($p < 0.01$), NATNH group was 4.83 ± 0.76 ($p < 0.01$), HK group was 7.13 ± 0.72 ($p < 0.01$), BVN group was 12.03 ± 1.72 ($p > 0.05$), and NS group 13.37 ± 1.54. All the p value was obtained comparison with the NS group.

Discussion

Targeting delivery has the advantage to enhance in the drug concentration in target tumor tissues. The main purpose of this work was to develop a novel drug delivery system, such as nanoparticles modified with folate loaded with HK that could improve the therapeutic efficacy of HK-based therapy on target tumor. HK has anti-inflammatory, anti-angiogenic, anti-oxidative properties, and anti-cancer property (Arora et al., 2012). However, the extreme water insolubility of HK hampers its delivering to the tumor at an effective concentration (Luo et al., 2008). Nanotechnology provides an interesting method to overcome water-solubility of hydrophobic drug (Allen & Cullis, 2004). We evaluated through HPLC the concentration of HK encapsulated in ATNH after adequately dissolved in deionized water at room temperature. The concentration of HK encapsulated in ATNH was approximately 0.54 mg/mL in water at room temperature, which was approximately 10 times more than the solubility of HK in water. Thus, HK water solubility was increased after encapsulation into nanoparticles.

Usually, PCEC nanoparticles have a core-shell structure with hydrophobic PCL-core and hydrophilic PEG shell. The hydrophobic core can act as a depot for many hydrophobic drugs, while hydrophilic PEG shell makes nanoparticles stable and long-circulating (Gou et al., 2009). Thus, in this report, we developed a targeting-FR drug delivery nanoparticles system using PCEC. In addition, in our previous report, we successfully showed that, FA-conjugated MPEG-PCL possesses excellent physical properties for targeting drug delivery (You et al., 2016). In this study, the vehicle we developed using PCEC showed many advantage such as high encapsulation efficiency for HK and the sustained and steady release behavior.

In this work, our results showed that ATNH loading hydrophobic HK not only overcome HK poor solubility but also the hydrodynamic diameter of the nanoparticles we obtained allowed them to avoid renal filtration during circulation in the human body, thus increasing the blood circulation time and facilitating effective targeting of the tumor through the EPR effect (Xu et al., 2015). However, the great disparity in size determined by TEM and DLS indicated differences between different methodologies. A remarkable difference in nanoparticles size obtained through TEM or DLS has been reported for other HK-loaded NPs and could be the result of the dehydration and/or the existence of aggregation (Gou et al., 2008, 2009, 2010).

The cytotoxicity results showed a reduced cell viability of tumor cells due to ATNH. However, BVN showed a negligible cytotoxic effect. These evidences suggested that ATNH inhibitory effect was attributed to the HK which encapsulated in it. Furthermore, the uptake into HNE-1 cell of the folate conjugated nanoparticles was more remarkable. Moreover, lower fluorescent intensity was observed following the addition of free folate into the medium than without folate, which demonstrated our hypothesis that HNE-1 cells active endocytose of the HK-loaded nanoparticles was FR mediated. These results indicated that ATNH remarkable inhibited cancer cell growth through delivering more HK into HNE-1 cells via folate-mediated endocytosis, while the carrier BVN could be considered as a safe drug deliver agent since it played a negligible cytotoxic effect. This was in accordance with the evidence that HK can inhibit cancer cell growth in a concentration dependent manner.

Although HK antitumor effects might not be explained by a single mechanism, our results clearly showed multiple antitumor pharmacological effects leading to cell cycle arrest, apoptosis, micro-vessels production, and proliferation suppression (Hahm & Singh, 2007; Fang et al., 2009; Cheng et al., 2016). Previous studies showed that HK can inhibit carcinoma cells growth through inducing G_0/G_1 phase cell cycle arrested (Arora et al., 2011; Chen et al., 2016; Hahm et al., 2016). Our cell-cycle study showed that ATNH remarkable increased the number of cells in G_1 phase, as shown by precious studies. In addition, apoptosis is a form of programed cell death and plays a vital role in drug treatment. HK had been shown to induce apoptosis in various types of cancer cells through inhibition of several well-known surgical/proliferation signaling pathways such as JAK/STAT.PI3K/Akt and MEK/Erk (Park et al., 2009; Zhang et al., 2014). Our work showed that the ATNH can remarkable increase the cancer cell apoptosis. Furthermore, angiogenesis plays a vital role in tumor growth and metastases (Hwang-Bo et al., 2012). Previous studies suggested that HK can exert anti-angiogenic effects through its potent anti-proliferative activity against endothelial cells. CD31 is an endothelial cell surface molecule that can be used to visualize MVD. Therefore, we detected the express of CD31 to confirm if the MVD in tumor tissue is suppressed. In addition, Ki 67 is a cell nuclear-antigen associated with cancer cell proliferation, as shown in many studies (Wang et al., 2014; Cheng et al., 2016). A recent study found that HK inhibits human U373 cell proliferation and induces apoptosis through p21/Cipl and p27/Kipl induction *in vitro* (Chen & Lee, 2013). Thus, our results showing a remarkable suppression of both CD 31 and Ki 67 in the ATNH-treated xenograft tumor tissues than other groups, suggested that the ATNH we developed was a potent angiogenesis and proliferation inhibitor. This Ki 67 and CD

31 significantly reduced expression might be due to the HNE-1 cells active targeting uptake the ATNH to form a high concentration of HK in the HNE-1 cells.

^{18}F-FDG PET/CT is widely used for tumor detection, as well as for monitoring a therapy, according to the Warburg Effect that underlines a basic difference between normal cells and cancer cells in glucose metabolism. Because ^{18}F-FDG is an analog of glucose, it is taken up by the cells via the glucose transporter and phosphorylated by the hexokinase. However, it is not further processed and remains trapped in the cells. Hence, its accumulation is an indicator of a high glucose uptake and hexokinase activity in tissues such as brain and brown fat. However, a higher FDG uptake in a given tumor may indicate an increased in the metabolism of glucose, suggesting a poor response and prognosis. On the other hand, tumors with a lower FDG uptake may tend toward a better response to treatment. Thus, a lower ^{18}F-FDG uptake observed in the groups bearing the tumor compared with the control groups might suggest that HK was more effective on suppressing the tumor metabolism.

Taken together, ATNH had remarkable activities to inhibit the HNE-1 cells growth both *in vivo* and *in vitro*. The main purpose of this work was to develop and demonstrate the active targeting drug delivery system loaded HK. We will study the biocompatibility, the toxicity, and the tissue distribution of the drug delivery system in the further study.

Conclusion

ATNH was successfully synthesized and could successfully target tumor cells both *in vitro* and *in vivo*. Thus, it might represent a promising potential NPC treatment due to its ability to induce cell apoptosis, cell cycle arrest at G_1 phase, and suppression of cell proliferation, micro-vessel generation, and tumor metabolism.

Acknowledgements

This work was supported by the Union Project of Luzhou City and Southwest Medical University under Grants [14JC0144 and 2013LZLY-J40]; Science and Technology Project of Luzhou City under Grant [2013-134] and Youth Talent Fund of the Affiliated Hospital of Southwest Medical University under Grant [2013-60].

Declaration of interest

The authors report no conflicts of interest in this work.

References

Allen TM, Cullis PR. (2004). Drug delivery systems: entering the mainstream. Science 303:1818–22.

Arora S, Bhardwaj A, Srivastava SK, et al. (2011). Honokiol arrests cell cycle, induces apoptosis, and potentiates the cytotoxic effect of gemcitabine in human pancreatic cancer cells. PLoS One 6:e21573.

Arora S, Singh S, Piazza GA, et al. (2012). Honokiol: a novel natural agent for cancer prevention and therapy. Curr Mol Med 12:1244–52.

Chen HC, Hsu HT, Weng JW, et al. (2016). Combined effect of honokiol and rosiglitazone on cell growth inhibition through enhanced G0/G1 phase arrest in hepatoma cells. J Chin Med Assoc 79:415–21.

Chen L, Hu CS, Chen XZ, et al. (2012). Concurrent chemoradiotherapy plus adjuvant chemotherapy versus concurrent chemoradiotherapy alone in patients with locoregionally advanced nasopharyngeal carcinoma: a phase 3 multicentre randomised controlled trial. Lancet Oncol 13:163–71.

Chen LC, Lee WS. (2013). P27/Kip1 is responsible for magnolol-induced U373 apoptosis *in vitro* and *in vivo*. J Agric Food Chem 61: 2811–19.

Cheng YC, Hueng DY, Huang HY, et al. (2016). Magnolol and honokiol exert a synergistic anti-tumor effect through autophagy and apoptosis in human glioblastomas. Oncotarget 7:29116–30.

Cho JH, Jeon YJ, Park SM, et al. (2015). Multifunctional effects of honokiol as an anti-inflammatory and anti-cancer drug in human oral squamous cancer cells and xenograft. Biomaterials 53:274–84.

Deng J, Qian Y, Geng L, et al. (2008). Involvement of p38 mitogen-activated protein kinase pathway in honokiol-induced apoptosis in a human hepatoma cell line (hepG2). Liver Int 28:1458–64.

Fang F, Gong C, Qian Z, et al. (2009). Honokiol nanoparticles in thermosensitive hydrogel: therapeutic effects on malignant pleural effusion. ACS Nano 3:4080–8.

Fried LE, Arbiser JL. (2009). Honokiol, a multifunctional antiangiogenic and antitumor agent. Antioxid Redox Signal 11:1139–48.

Fu SZ, Wang XH, Guo G, et al. (2011). Preparation and properties of nano-hydroxyapatite/PCL-PEG-PCL composite membranes for tissue engineering applications. J Biomed Mater Res B Appl Biomater 97: 74–83.

Gou M, Gong C, Zhang J, et al. (2010). Polymeric matrix for drug delivery: honokiol-loaded PCL-PEG-PCL nanoparticles in PEG-PCL-PEG thermosensitive hydrogel. J Biomed Mater Res A 93:219–26.

Gou M, Li X, Dai M, et al. (2008). A novel injectable local hydrophobic drug delivery system: Biodegradable nanoparticles in thermo-sensitive hydrogel. Int J Pharm 359:228–33.

Gou M, Zheng L, Peng X, et al. (2009). Poly(epsilon-caprolactone)-poly(ethylene glycol)-poly(epsilon-caprolactone) (PCL-PEG-PCL) nanoparticles for honokiol delivery *in vitro*. Int J Pharm 375:170–6.

Hahm ER, Singh KB, Singh SV. (2016). c-Myc is a novel target of cell cycle arrest by honokiol in prostate cancer cells. Cell Cycle 15: 2309–20.

Hahm ER, Singh SV. (2007). Honokiol causes G0-G1 phase cell cycle arrest in human prostate cancer cells in association with suppression of retinoblastoma protein level/phosphorylation and inhibition of E2F1 transcriptional activity. Mol Cancer Ther 6:2686–95.

Huang Y, Yang T, Zhang W, et al. (2014). A novel hydrolysis-resistant lipophilic folate derivative enables stable delivery of targeted liposomes *in vivo*. Int J Nanomedicine 9:4581–95.

Hwang-Bo J, Yoo KH, Park JH, et al. (2012). Recombinant canstatin inhibits angiopoietin-1-induced angiogenesis and lymphangiogenesis. Int J Cancer 131:298–309.

Jeong JJ, Lee JH, Chang KC, Kim HJ. (2012). Honokiol exerts an anticancer effect in T98G human glioblastoma cells through the induction of apoptosis and the regulation of adhesion molecules. Int J Oncol 41:1358–64.

Li Z, Liu Y, Zhao X, et al. (2008). Honokiol, a natural therapeutic candidate, induces apoptosis and inhibits angiogenesis of ovarian tumor cells. Eur J Obstet Gynecol Reprod Biol 140:95–102.

Liu H, Zang C, Emde A, et al. (2008). Anti-tumor effect of honokiol alone and in combination with other anti-cancer agents in breast cancer. Eur J Pharmacol 591:43–51.

Luo H, Zhong Q, Chen LJ, et al. (2008). Liposomal honokiol, a promising agent for treatment of cisplatin-resistant human ovarian cancer. J Cancer Res Clin Oncol 134:937–45.

Park EJ, Min HY, Chung HJ, et al. (2009). Down-regulation of c-Src/EGFR-mediated signaling activation is involved in the honokiol-induced cell cycle arrest and apoptosis in MDA-MB-231 human breast cancer cells. Cancer Lett 277:133–40.

Shi F, Yang G, Ren J, et al. (2013a). Formulation design, preparation, and *in vitro* and *in vivo* characterizations of beta-Elemene-loaded nanostructured lipid carriers. Int J Nanomedicine 8:2533–41.

Shi J, Zhang H, Wang L, et al. (2013b). PEI-derivatized fullerene drug delivery using folate as a homing device targeting to tumor. Biomaterials 34:251–61.

Shi S, Shi K, Tan L, et al. (2014). The use of cationic MPEG-PCL-g-PEI micelles for co-delivery of Msurvivin T34A gene and doxorubicin. Biomaterials 35:4536–47.

Singh T, Gupta NA, Xu S, et al. (2015). Honokiol inhibits the growth of head and neck squamous cell carcinoma by targeting epidermal growth factor receptor. Oncotarget 6:21268–82.

Torre LA, Bray F, Siegel RL, et al. (2015). Global cancer statistics, 2012. CA Cancer J Clin 65:87–108.

Wang T, Chen F, Chen Z, et al. (2004). Honokiol induces apoptosis through p53-independent pathway in human colorectal cell line RKO. World J Gastroenterol 10:2205–8.

Wang X, Beitler JJ, Wang H, et al. (2014). Honokiol enhances paclitaxel efficacy in multi-drug resistant human cancer model through the induction of apoptosis. PLoS One 9:e86369.

Xie M, zhang H, Xu Y, et al. (2013). Expression of folate receptors in nasopharyngeal and laryngeal carcinoma and folate receptor-mediated endocytosis by molecular targeted nanomedicine. Int J Nanomedicine 8:2443–51.

Xu Z, Liu S, Liu H, et al. (2015). Unimolecular micelles of amphiphilic cyclodextrin-core star-like block copolymers for anticancer drug delivery. Chem Commun (Camb) 51:15768–71.

You H, Fu S, Qin X, et al. (2016). A study of the synergistic effect of folate-decorated polymeric micelles incorporating Hydroxycamptothecin with radiotherapy on xenografted human cervical carcinoma. Colloids Surf B Biointerfaces 140:150–60.

Younes-Mhenni S, Janier MF, Cinotti L, et al. (2004). FDG-PET improves tumour detection in patients with paraneoplastic neurological syndromes. Brain 127:2331–8.

Zhang Q, Zhao W, Ye C, et al. (2015a). Honokiol inhibits bladder tumor growth by suppressing EZH2/miR-143 axis. Oncotarget 6: 37335–48.

Zhang Y, Chen T, Yuan P, et al. (2015b). Encapsulation of honokiol into self-assembled pectin nanoparticles for drug delivery to HepG2 cells. Carbohydr Polym 133:31–8.

Zhang Y, Ren X, Shi M, et al. (2014). Downregulation of STAT3 and activation of MAPK are involved in the induction of apoptosis by HNK in glioblastoma cell line U87. Oncol Rep 32: 2038–46.

Zheng X, Kan B, Gou M, et al. (2010). Preparation of MPEG-PLA nanoparticle for honokiol delivery *in vitro*. Int J Pharm 386:262–7.

Zhou YY, Du YZ, Wang L, et al. (2010). Preparation and pharmacodynamics of stearic acid and poly (lactic-*co*-glycolic acid) grafted chitosan oligosaccharide micelles for 10-hydroxycamptothecin. Int J Pharm 393:143–51.